An efficient numerical approach to the prediction of laminate tolerance to Barely Visible Impact Damage

Abrar H. Baluch[1a], Olben Falcó[a], José Luis Jiménez[a], Bas H. A. H. Tijs[b], Cláudio S. Lopes[1a]

[a]*IMDEA Materials Institute, c/ Eric Kandel 2, 28906 Getafe, Madrid, Spain*
[b]*GKN Aerospace: Fokker, Papendrecht, The Netherlands*

Abstract

An efficient numerical approach for the prediction of the Compression After Impact (CAI) strength of aerospace-grade CFRP laminates when exposed to Barely Visible Impact Damage (BVID) is proposed. The approach is based on mapping relevant BVID features, i.e. delaminations, onto an efficient CAI finite element model based on continuum shell discretization, and can be used on Low-Velocity Impact (LVI) results obtained experimentally or by means of high-fidelity virtual tests. It is proposed that delaminations may be represented by simplified shapes, and only the ones at critical through-thickness locations need to be mapped, allowing the clustering of several plies in a single shell layer. General guidelines, that are potentially valid for a wide range of unidirectional CFRP laminates, are proposed to identify relevant and critical BVID features to be mapped onto the efficient CAI modelling. The approach was validated for five laminates of AS4/8552 material, covering a range of different thicknesses, overall achieving CAI strength predictions within 5% of the experimental results. In comparison with the alternative high-fidelity CAI virtual testing approach, this method leads to computational efficiency gains of an order of magnitude. Moreover, the full simulation of the sequence LVI plus CAI steps can be accelerated by a factor of four.

Keywords: Virtual Testing, Low-Velocity Impact (LVI), Compression After Impact (CAI), Barely Visible Impact Damage (BVID)

---

[1]Corresponding authors: abrar.baluch@imdea.org, claudiosaul.lopes@imdea.org

1. Introduction

The usage of laminated composite materials is increasing exponentially in all engineering sectors, specially aerospace and automotive, wherein they allow many advanced structures with desirable properties which were otherwise not possible. However, such structures also have unique ways towards failure [1–3]. Their failure mechanisms vary according to the loading scenario and include fiber breakage and kinking, matrix cracks and delamination. The contribution of these mechanisms towards damage also varies according to the loading type and direction. One sensitive aspect for aerospace composite structures is the event of Low-Velocity Impact (LVI) that leads to Barely Visible Impact Damage (BVID). The circumstances leading to BVID vary widely, from dropped tools on composite panels to in-service impacts, among other reasons. This type of damage plays a critical role in the structural integrity of composite structures, mainly because of its difficult identification. BVID consists mostly in local delamination, hidden from the naked eye underneath a possibly unsuspected impact point, that can have a critical detrimental effect on the strength of composite structures when in-service.

The mechanisms of initiation and progression of delamination in LVI events have been described in the literature [4–7]. Hull et al. [8] observed that delaminations tend to develop along major axes parallel to the fiber orientation of he neighbouring ply furthest away from the impact point, and that their area is highly dependent on the specimen out-of-plane displacement during impact. Such damage then has the major contribution towards laminate failure in the event of Compression After Impact (CAI) loads. This is fundamentally because of the reduction of structural stability caused by the delaminated composite. The CAI event can reduce the component strength up to 60% in comparison to pristine samples [9–13]. Therefore, the CAI strength is considered a critical design parameter for a large number of aircraft structures, and it has been standardized to assess the tolerance to BVID in composite laminates.

The CAI strength of composite laminates affected by BVID depends on delamination and its characteristics, including geometry, size and orientation, as well as on its location through the thickness of the composite [14–16]. In support of there assertions, experimental studies have been carried out by means of artificially generated delaminations, with different shapes, and at different locations through the thickness of composites [17, 18]. Multiple delamination configurations have been explored in the literature. Some researchers used circular delaminations [19] with regular intervals, while some others used elliptical shapes, and yet a fewer others used peanut-shaped, which is claimed to be a more realistic profile [16]. Wang et al. [20] reported that the distribution of delaminations at different locations through thickness of laminates severely affects their CAI strength. Aslan et al. [21] reported that delamination at interfaces near the laminate surface resulted in the highest reductions of the CAI strength. In fact, it has been proposed that a single circular delamination near the surface dominates the CAI response [22]. Minak et al. [23] discussed in detail the effects of intra-ply matrix cracking, and its interaction with interface delamination propagation, on the CAI response of thick and thin laminates. At present, most of the researchers agree that the influence of matrix cracking on the tolerance to BVID is negligible compared to the effect of delamination.

A substantial number of researchers have studied multiple BVID configurations and developed analytical and semi-analytical CAI strength reduction models [1, 14, 15, 18, 22, 24–27] based on one or more through-thickness delaminations of idealized shapes. Judging by one of the recent works [22], besides their readiness and efficiency, such models can be accurate to within 30-40% error bounds.

To obtain the delamination profile on impacted laminated specimens, the most straight-forward way is to measure it experimentally by conducting ultrasonic inspection (C-scan). Alternatively, the capabilities to predict the delaminated surfaces with substantial accuracy have been developed in recent years and go by the mark of virtual testing, i.e. high-fidelity finite element (FE) simulations [28–31]. Notwithstanding their disputable accuracy, the virtual testing approach to LVI has the advantage that it can straightforwardly include the simulation of the CAI event as a follow-up simulation step, as proposed in [29, 30], and be used for BVID resistance and tolerance predictions. However, the high-fidelity simulation of both loading steps can be quite expensive computationally, as will be shown in this paper.

In this work, an efficient numerical methodology to accurately predict tolerance to BVID is proposed and validated. The approach can be seen as an alternative to the expensive CAI simulations, and can be applied on results of either experimental or high-fidelity simulations of LVI. It consists on mapping relevant BVID features, i.e. delaminations, onto an efficient CAI finite element model based on continuum shell discretization. To aide the development and validation of the methodology, LVI and CAI experiments were carried on different laminate configurations based on the AS4/8552 carbon fibre-reinforced material system. Nonetheless, the guidelines proposed in this paper to perform delamination mapping into efficient CAI modelling are potentially applicable to a wide range of composite laminates. The applicability of the proposed methodology is, however, limited to impact configurations that are dominated by delamination.

2. Experimental evaluation of laminate tolerance to BVID

This section describes the LVI experiments that were performed to acquire the BVID data on different specimens, as well as the CAI tests to validate the proposed damage tolerance assessment methodology.

2.1. Test specimens

Unidirectional AS4/8552 pre-preg material was used to manufacture five different kinds of laminates. These configurations were selected on the basis of their use in aerospace applications at industrial level. The configurations constitute limits of the design space in terms of stiffness properties. This is reflected in the following approximate percentage ratios of plies in the 0, ±45, and 90 directions which are used in the aerospace industry for configuration identification: 30/60/10 (361); 30/50/20 (351); 25/50/25 (252); and 10/80/10 (181 and 181T). The laminates were cured in autoclave by adopting standard procedures at GKN Aerospace: Fokker. Their stacking sequences and average ply properties are presented in Tables 1 and 2 respectively.

Table 1: Laminate configurations analyzed.

Laminate	**# of plies**	**thick [mm]**	**Stacking Sequence**	**0° plies %**	**45° plies %**	**90° plies %**
181	16	2.944	$[\pm 45/0/45_2/-45_2/90]_S$	12.5	75.0	12.5
181T	20	3.68	$[\pm 45/0/\pm 45/90/\pm 45_2]_S$	10.0	80.0	10.0
252	24	4.416	$[(45/0/\text{-}45/90)_3]_S$	25.0	50.0	25.0
351	24	4.416	$[45/0/\text{-}45/0/45/0/\text{-}45/90/45/90/\text{-}45/0]_S$	33.0	50.0	17.0
361	34	6.256	$[45/0/\text{-}45/0/\pm 45/0/-45/90/45_2/90/-45/0_2/\pm 45]_S$	30.0	60.0	10.0

Table 2: Average AS4/8552 ply material properties (taken from [32]).

Ply elastic properties						
E_{1t} (GPa)	E_{1c} (GPa)	E_{2t} (GPa)	E_{2c} (GPa)	$G_{12} = G_{13}$ (GPa)	$v_{12} = v_{13}$	v_{23}
137.1	114.3	8.8	10.1	4.9	0.314	0.487
Ply strengths properties						
X^{T} (MPa)	X^{C} (MPa)	Y^{T} (MPa)	Y^{C} (MPa)	S^{L} (MPa)		
2106.4	1675.9	74.2	322.0	110.4		
Interface properties						
τ_n^0 (MPa)	τ_{sh} (MPa)	$G_{\mathrm{Ic},\theta=0}$ (kJ/m^2)	$G_{\mathrm{IIc},\theta=0}$ (kJ/m^2)	η_{bk}		
74.2	110.4	0.30 ± 0.01	0.87 ± 0.06	1.45		

2.2. Barely Visible Impact Damage (BVID)

The pristine specimens were subjected to drop-weight impact experiments according to the Airbus standard test method AITM 1-0010 and ASTM D7136 [33, 34] by means of a CEAST 9350 Drop Tower Impact System (Instron). Different impact energies,in the range of 10J to 70J, were experimented in order to determine the threshold of BVID. At least two repetitions of each impact test were performed. The permanent indentation on each specimen was measured after 30 min of the impact event by using a depth gauge. The compiled results are shown in curves of increasing indentation depth for increasing impact energy (Figure 1). For each configuration, interpolation was performed to estimate the energy corresponding to the threshold of BVID, defined by the test standard as relating to a permanent indentation of 1 mm [35–37]. This criterion establishes that an impact event is identifiable when the resulting permanent indentation is deeper than 1 mm. Three impact test per configurations were then performed at approximately those energies and the corresponding results added to the database (Figure 1).

From this point onward, the presented research focus on the impact configurations corresponding to the determined energy threshold for BVID. The proposed analysis methodology can only be considered valid for impact damage dominated by delamination, such as BVID.

Non-Destructive Testing (NDT) was conducted on the samples impacted at the thresholds of BVID to analyze the extent of damage. To determine the impact damage footprint, i.e. the superposition of all damage features in the specimens, the technique of ultrasonic C-scan (Tecnitest Triton 1500 USPC-

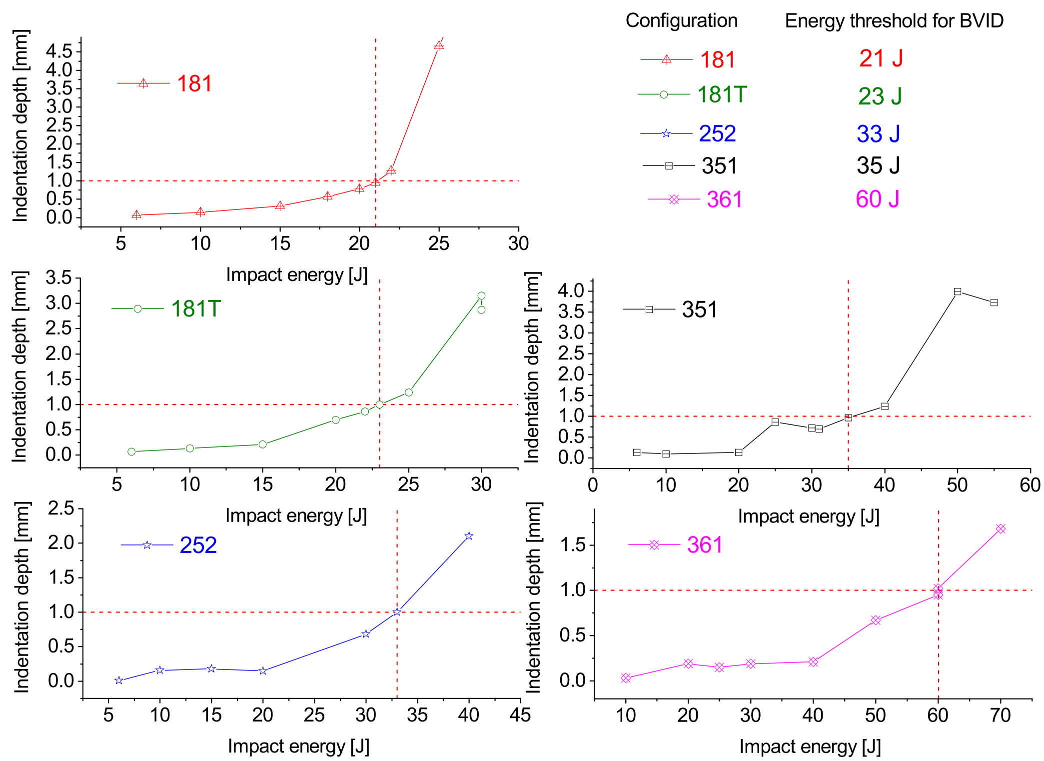

Figure 1: Experimentally-obtained relations between impact energy and permanent indentation for all configurations analyzed, and identification of BVID threshold.

3100 ultrasonic) was employed. An attenuation of 12 db was established as the threshold of damage. The location of delaminations through the thickness of the laminate was also determined by means of the same ultrasound equipment in depth scan mode. Such depth scans were performed on both faces of the samples, impact and back (opposite-to-impact) sides, with results shown in Figure 2. For all cases, a delamination can be observed a the ply furthest away from the impact point. Moreover, these delaminations have approximately oval shape with a large aspect ratio and major axis aligned with the fibre orientation of the delaminated ply. This phenomenon has been extensively reported in the literature and is due to back-face splitting (see Figure 8). From the impact face, the first major delamination was found always at a depth over 1 mm. At shallower depths, major delaminations were suppressed by high out-of-plane compressive stresses [38]. For the inner specimen interfaces, delaminations seem to be bounded by circumferences of approximately constant diameter.

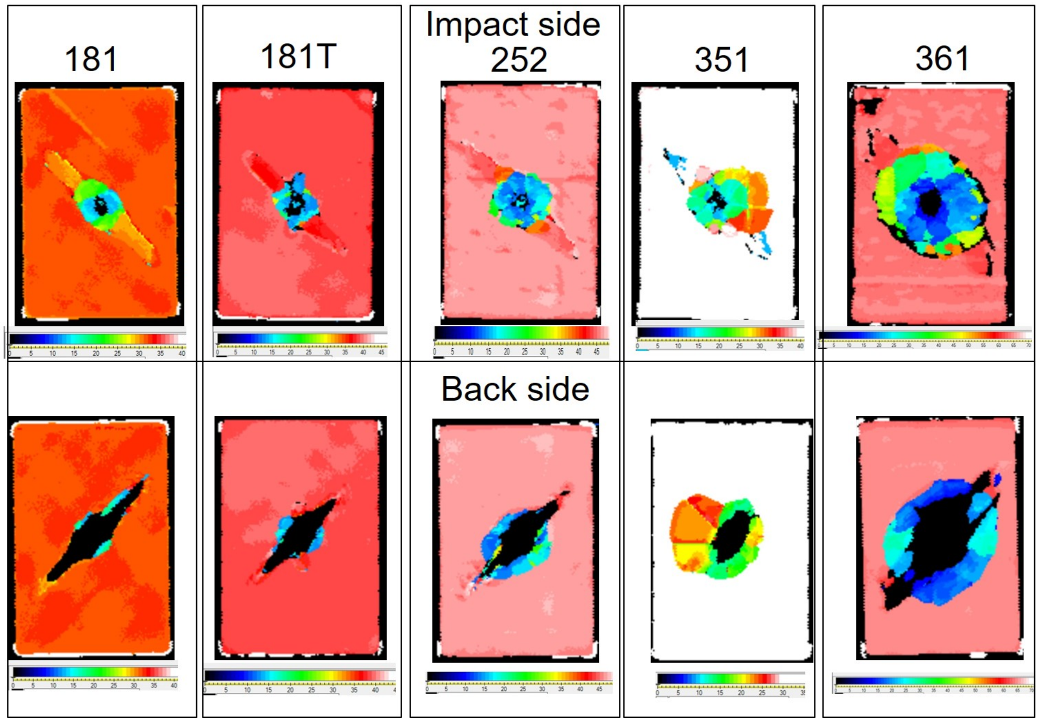

Figure 2: Depth scan for multiple laminates after BVID. The colour scheme at bottom of each figure represents the depth of delamination (scale: x0.1 mm).

2.3. Damage tolerance

In order to determine the tolerance to BVID, standard Compression After Impact (CAI) tests were performed on three specimens of each configuration following the procedures defined by ASTM D7137 and AITM 1-0010 [34, 39], using an electromechanical testing machine (Instron 3384) equipped with a 150 kN load-cell in combination with an anti-buckling support fixture. To monitor out-of-plane displacements and correct eventual global buckling behaviour, a Digital Image Correlation (DIC) system was used (VIC-3DTM, Correlated Solutions). The failed specimens were then again analyzed by means of ultrasonic C-Scan to determined the delamination patterns resultant of the CAI tests.

The results of the CAI tests in terms of specimen deformation and superimposed delamination patterns can be appreciated in Figure 8. A significant amount of damage to the backface plies is visible, mainly in the form of ply splitting. The average experimentally-obtained CAI strength values are represented in Figure 9.

3. State-of-the-art virtual testing of BVID and CAI

As pointed out in the introduction, high-fidelity simulations have been proposed by different authors [28–31] to predict the LVI and CAI behaviours of composite laminates. Two-step analyses were proposed to describe both loading cases in sequence [29, 30]. The first step tackles the simulation of LVI. Once it finishes, after enough physical time to allow for the rebound of the impactor plus the dissipation of major vibrations in the virtual specimen (typically requiring 5 to 10% of the total contact time), a second step ensures addressing the simulation of the CAI. This type of approach was also pursued in this work. The purpose was twofold. On the one hand, the high-fidelity simulation of LVI was as a way to predict the threshold of BVID in all analyzed specimens with high realism without having to conduct experiments. On the other hand, the high-fidelity simulation of compression after BVID was used in order to establish a reference case for comparison against a more efficient approach proposed in this research. Hence, the simulation of CAI using this method was conducted only for one of the laminate configurations.

3.1. Modelling approach

FE modelling of the composite coupons were carried out in Abaqus/Explicit [40], following the methodology proposed in [28] and briefly described as follows. The virtual standard coupons were split into parts employing different discretization levels, and whose kinematic compatibility was ensured by means of tie constraints, as proposed earlier by the authors [32]. A global discretization was employed to the coupon end sections by using continuum shell elements describing the linear-elastic laminate behaviour. The central damage zone, where the possibility of damage is taken into account, used three-dimensional ply-by-ply discretization (with reduced-integration C3D8R elements in Abaqus [40]).

Delamination and intraply damage mechanisms were tackled by two distinct approaches. The ply damage model was based on the work of Maimí et al. [41, 42], ensuring the correct dissipation of energy associated with different ply failure modes, and was implemented by means of a VUMAT user subroutine. Ramberg-Osgood laws [43] were used to describe the material nonlinear shear responses. The onset of ply damage was determined by means of the three-dimensional failure criteria proposed by Catalanotti et al. [44], and it was followed by exponential damage laws. Matrix cracking was assumed to occur under mixed-mode behaviour. To enable delamination among different plies, the surface-based cohesive zone modelling approach implemented in Abaqus [40] was employed. This allowed the description of inter-ply damage and ply decohesion by means of a generalized traction-separation behavior [45] in combination with a general contact algorithm applied to ply surfaces. Frictional contact among delaminated plies was simulated by coupling a Coulomb-type model (μ =0.5) to the cohesive zone formulation. The interface penalty stiffness was set to 2x10^5 N/mm^3 in all traction directions, after checking that it provided correct results while allowing efficient computations. Delamination initiation was predicted by a quadratic interactive stress criterion while the propagation of this damage mode was tacked with the energy-based Benzeggagh-Kenane (BK) criterion [46].

The mesh generation was governed by mesh alignment with orthotropic material directions and directional biasing (mesh ratio of 3 to 1), as proposed in [32]. Moreover, the mesh regularization approach proposed by Baẑant and Oh [47] was employed to ensure the proper computation of the crack energy release rate for each damage mode. The application of this regularization scheme imposes severe limits to the maximum element dimensions, and this leads to element counts in excess of 1.5 million for a typical LVI-CAI specimen.

The described two-step modelling approach is schematically illustrated in Figure 3. Of crucial importance is the application of the appropriate boundary conditions in each step. These were applied by explicitly modelling the contacts between the specimens and supporting fixtures. In the LVI step, four clamps and a rigid support with a central window interacted with the specimen by means of contact interactions with friction, allowing also to absorb oscillations after rebound of the rigid impactor. For the simulation of the CAI step, two new fixture parts, loading plates and side fixture plates, were put in contact with the composite specimen, as shown in Figure 3. While the side fixture plates and one of the loading plates were prevented of movement during the CAI step, a gradual compressive displacement was imposed to the remaining loading plate.

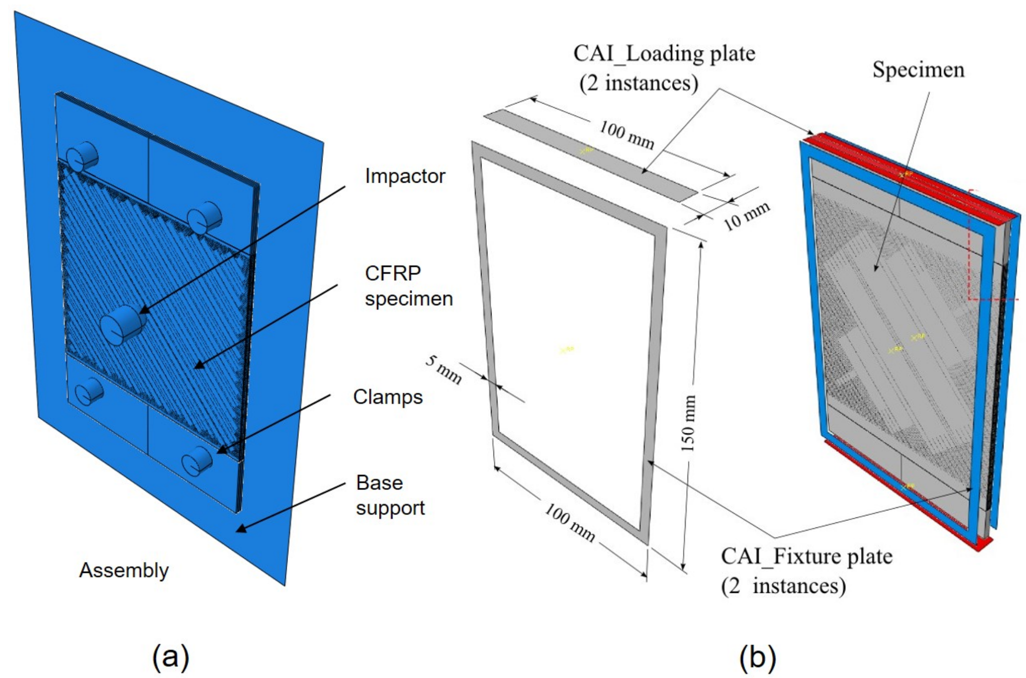

Figure 3: Details of high-fidelity simulation of BVID tolerance: (a) LVI virtual test set-up. (b) CAI virtual test set-up.

A velocity speed-up factor was applied to the CAI loading in order to improve the efficiency of the computational analyses while keeping quasi-static loading conditions, i.e. that the kinetic energy ($E_k = 1/2MV^2$) is relatively small (typically $< 5\%$) compared to the overall specimen internal energy.

3.2. Results and limitations of the approach

As a reference case, the two-step LVI+CAI simulation process for 181 configuration impacted at the threshold of BVID (21J) is schematically depicted in Figure 4. It can be observed that the delamination profile is fully developed at about half of the LVI step, corresponding to the peak impact load. Such behaviour has been observed in earlier works [30, 31], and is due to the quasi-static nature of the LVI event. Moreover, the LVI delamination profile does not grow further until the peak compression load point in the CAI step, at which stage it rapidly propagates towards the edges of the sample causing its unstable crushing associated with sublaminate buckling.

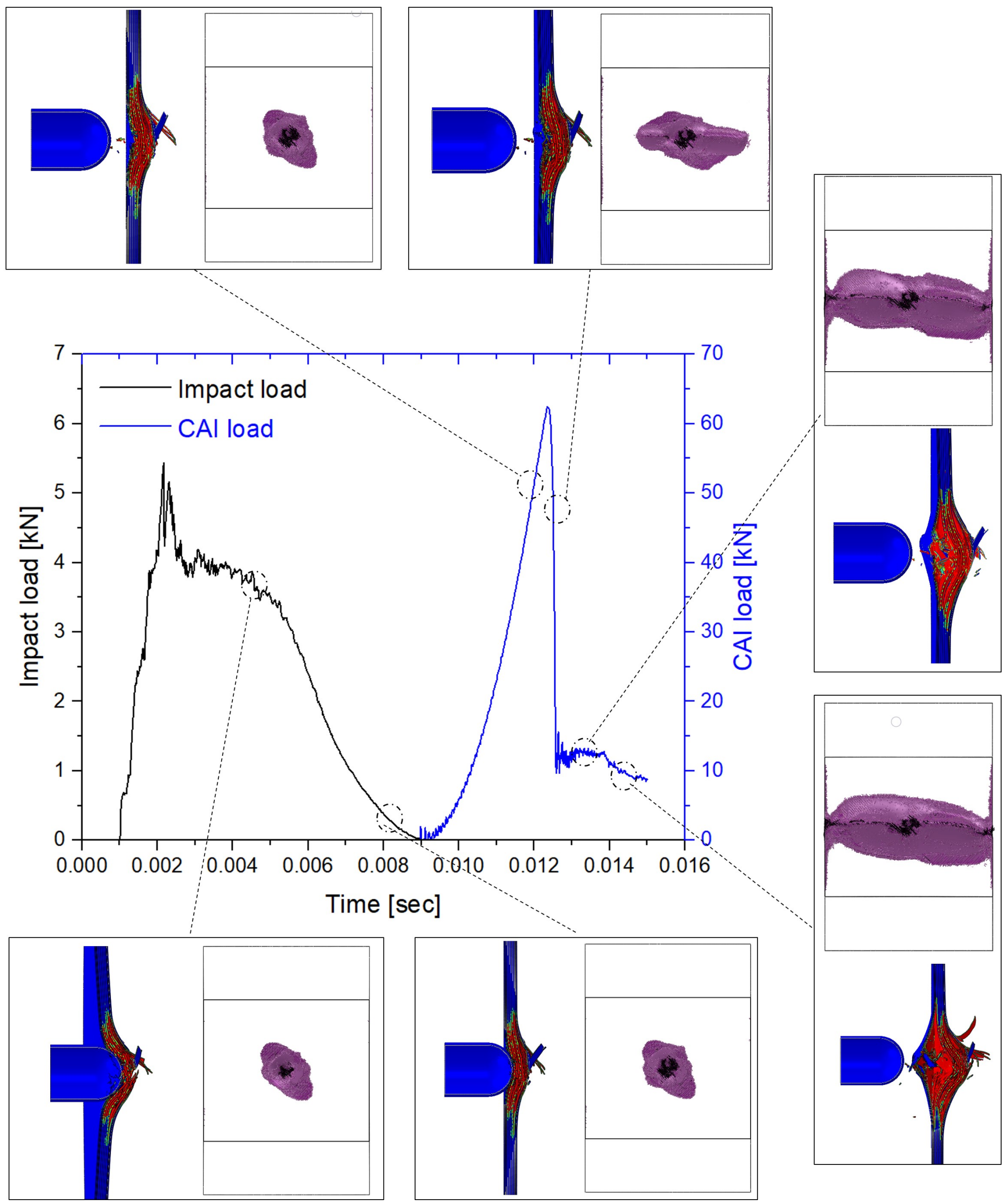

Figure 4: Schematics of the LVI+CAI virtual testing on the 181 configuration impacted at the threshold of BVID (21J).

Although this modelling approach provides high-fidelity results as well as very good insights on the development of BVID, its propagation under compression loads and eventually good predictions of damage tolerance, it is very expensive computationally. The two-step simulation represented in Figure 4 took in excess of 100 hours to process in 48 parallel computing cores (6x Intel Xeon IvyBridge 2.5GHz CPU). The CAI step alone took around 50 hours. For samples with a higher number of plies, as in all the remaining configurations analyzed in this work, the computation time would increase proportionally due to higher number of elements, and would result unpractical.

4. Proposed methodology to predict tolerance to BVID based on damage mapping

It has been demonstrated that, for the range of BVID damage events, the induced intraply damage is limited and/or has negligible detrimental effect on compressive strength, i.e. the CAI behaviour after BVID depends almost exclusively on the delamination damage produced during LVI [48]. This is because the CAI response is dominated by the loss of stability due to the splitting of the specimen into sublaminates rather than by the loss of ply compressive strength produced by intralaminar damage which, in this range of impact energies, is mostly constituted by matrix cracks which can close under compression. In addition, it is assumed in this work that the permanent indentation in the range of BVID (< 1 mm) has negligible effect on such loss of stability as compared to the effect of the size of the produced delaminations.

The above-mentioned observation and assumption motivate possible substantial simplifications in the CAI modelling. On the one hand, no intraply damage model is needed, with the addition that the mesh requirements cease to be bounded by the limits imposed by the mesh regularization scheme. On the other hand, it may become possible to cluster several plies into a sublaminate modelled by a single through-thickness element, and account for delaminations only at certain critical interfaces. Hence, the efficient CAI modelling strategy proposed in this work consists on mapping relevant BVID features, i.e. delaminations, onto an efficient CAI finite element model based on continuum shell discretization. The approach can be seen as an alternative to the expensive CAI simulations that follow equally expensive high-fidelity LVI simulations, but can also be applied on experimental LVI results. Moreover, when applied on LVI virtual test results, it leads not only to a simplification of the CAI step but also of the required LVI process simulation since it does not need to include the rebound of the impactor, i.e. the LVI simulation only needs to be conducted up to maximum impact load point when the delamination profile gets to be fully developed.

4.1. Modelling approach

In contrast to the high-fidelity simulation approach described above, the efficient methodology proposed in this work to model CAI consists in the use of continuum shell elements (SC8R elements in Abaqus [40]) to model delaminated sublaminates. From the modelling point of view, these elements resemble three-dimensional elements, allowing for contact relations to be specified at different surfaces, however their constitutive behaviour is that of a conventional shell. This has the added advantage that the bending behaviour of plies and sublaminates is addressed with better accuracy than with three-dimensional elements.

Similarly to the high-fidelity simulation approach, the virtual coupons were split into parts employing different discretization levels, which were constrained kinematically by means of tie constrains, as shown in Figure 5. In the central zone, multiple sublaminates were created with surface contact relations between them. Delaminations resulting from BVID were modelled as circular or oval regions wherein only contact and friction conditions were specified between sublaminate surfaces. These were then allowed to propagate under CAI loads. This was achieved by using cohesive-frictional contact relations outside those pre-delaminated areas, in a similar way as defined in high-fidelity models. The meshing in this region was governed by the requirements of the cohesive modelling approach to achieve a reasonable description of the fracture process zone [49]. Within the regions away from the central sections, a coarser mesh was used in combination with a single continuum shell element through-the-thickness of the entire laminate. The total number of SC8R elements was in the order of 500.000, varying according to the laminate configuration analyses.

Standard CAI boundary conditions and loads were applied in simplified form, i.e. by applying nodal constraints and velocities instead of explicitly modelling the testing fixtures as required by the high-fidelity simulation approach. Both loading velocity speed-up and mass scaling (1000x) were used to improve the efficiency of the computational analyses while keeping quasi-static loading conditions similar to the high-fidelity CAI simulation approach

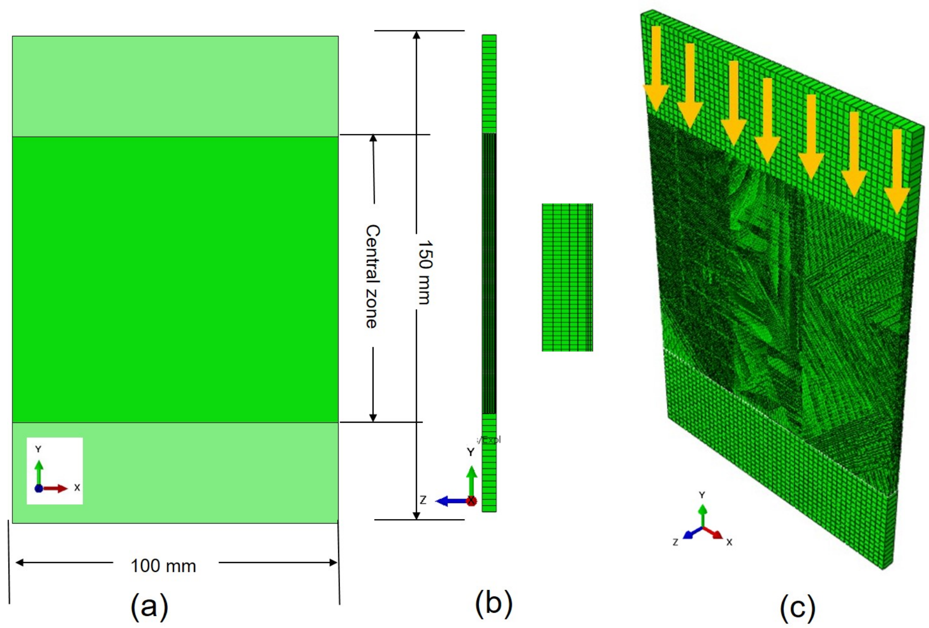

Figure 5: Specimen geometry as per ASTM D7137 and Airbus standard AITM 1-0010. (a) Front view. (b) Side view along with clustered plies. (c) CAI loading applied.

described above ($E_k < 5\%$ of specimen overall internal energy). As an example, the computation time necessary for the simulation of the CAI of the 181 configuration, using the same parallel computing configuration used for the high-fidelity analyses (48-core), was 8 hours on average, representing a speed-up factor of about 6.5 w.r.t. the high-fidelity virtual testing.

One further modelling simplification was also employed and validated, consisting in coarsening the mesh in the central region of the specimens behind the limits imposed by the nominal interface properties to guarantee accurate description of delamination initiation and propagation. According to recommendations given in the literature [49], a few cohesive elements are required to model appropriately the cohesive fracture process zone, whose length (l_{cz}) can be estimated with

$$l_{cz} = ME\frac{G_c}{(\tau^0)^2} \tag{1}$$

wherein E is the Young modulus of the material, G_c is the interface fracture energy release rate, τ^0 is the maximum interfacial strength (see Table 2), and

M is a model parameter which was proposed by Rice [50] to be 0.88. In this work, cohesive surfaces are used instead of cohesive elements, but a similar number of degrees of freedom within the fracture process zone is adopted to capture the fracture mechanism in a smooth progressive way. Considering the above guidelines and mesh convergence studies, an average element size of 0.4 mm was adopted.

According to the engineering solution for using coarse meshes in the simulation of delamination with cohesive zone models proposed by Turon et al. [49], the propagation of delamination can still be predicted with reasonable accuracy if l_{cz} is enlarged by lowering τ^0 while keeping G_c constant, as well as the other parameters in Equation 1. This approach is, however, likely to compromise the correct capturing of delamination initiation. Though, most problems involving delamination such as CAI are governed by its propagation instead by its initiation.

The application of the engineering solution for coarse meshes proposed by Turon et al. [49] to the current case allowed mesh coarsening from element lengths of 0.4 mm to 1.0 mm. The result, in terms of efficiency gain, was a reduction of the computation time by another factor of 8.1 w.r.t the baseline BVID mapping strategy, and an overall speed-up factor of 53 (the virtual CAI test of the 181 configuration took 45-50 minutes).

4.2. Simplified BVID mapping strategy

The damage footprints for all configurations impacted at the threshold of BVID, as determined by means of ultrasonic C-Scan inspection, are shown in Figure 6. The damage footprints roughly consist of the superimposition delaminations at each interface (see also Figure 2)

It is proposed that the performance of the virtual testing approach can be further increased, while maintaining effectiveness, by mapping only delaminations at a few critical interfaces. Supported by extensive research on typical delamination profile characteristics, related literature and experimental observations, multiple configurations were explored to provide the artificial maps of delamination in the samples impacted at the threshold of BVID.

It has been demonstrated that delamination size, depth location, predominat orientation, number of delaminated interfaces, as well as specimen dimensions, boundary conditions and stacking sequence affect CAI behaviour which is eventually dominated by the mechanisms of local sublaminate buckling and global laminate buckling [22, 25, 26, 51]. It was also found that the

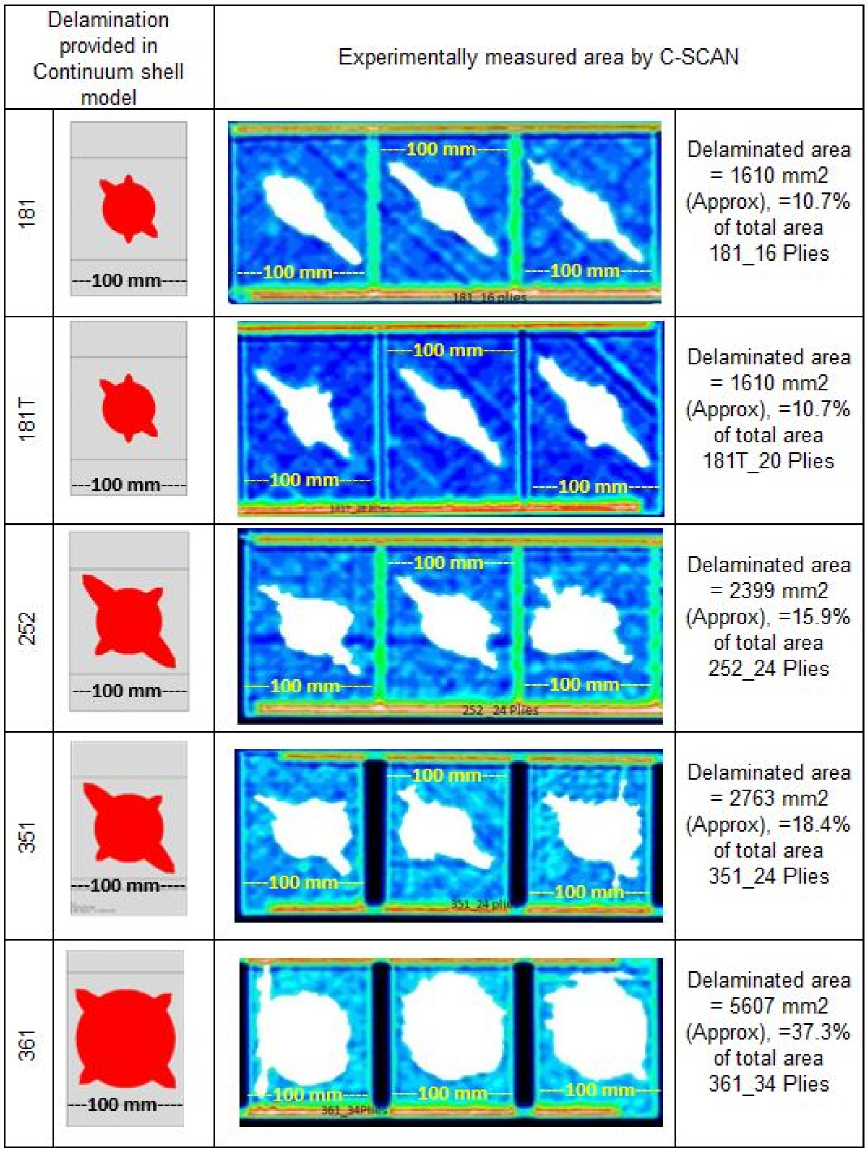

Figure 6: BVID profiles obtained by means of ultrasonic C-scan (three repetitions for each impact configuration). Simplified delamination mapping profiles are shown for comparison.

ratio of delamination width to laminate width has a significant effect on these buckling modes [52]. Hence, in the present research, sensitivity analyses were performed for different delamination sizes and geometries including circular, oval and peanut-shaped along with their location through the thickness of the laminate.

In previous research, near-surface delaminations were found to be critical for in CAI strength reduction [15, 22]. Single delaminations near to surface appeared to be more severe in comparison to multiple delaminations at the interior of laminate. Moreover, the strength reduction is more accentuated when the previous circumstance is combined with the existence of one or more of the external-most plies oriented in loading direction. In contrast, other studies pointed out that only delaminations located deeper than a critical depth of 10 to 20 % of the laminate thickness trigger the buckling phenomenon [53].

Based on the present and previous studies, a set of guidelines was established that is applicable to typical aerospace laminates, such as the ones analyzed in this work, and possibly many other configurations irrespective of the material system. The following guidelines can either be used with experimentally- or numerically-obtained data.

1. **The mapped delaminations should be represented either by circular or elliptical shapes, in the later case, aligned with the orientation of the neighbouring ply furthest away from the impact face.**

   The majority should be circular with diameter equal to the one of the smallest circumference that is able to encompass the BVID footprint (leaving out the effects of back-face splitting). Oval shapes should be used for mapped delaminations at ply interfaces close to the laminate surfaces, and have major axes parallel to the orientation of the innermost neighboring ply. The observation that the major axes of LVI-resulting delaminations match with the orientation of the neighbouring ply furthest away from the impact face was made by several authors, as for example Obdrz̄álek [24] Lopes et al. [5]. The dimensions of the ellipses should be made relative to the diameter of BVID footprint, as detailed below.

2. **Clustered plies should be modelled as unique thick plies, and delamination between those and inner neighbouring plies should always be mapped.**

   Delamination should not be allowed between clustered plies, which can be considered thick plies. However, under LVI loads, thick plies induce high interlaminar shear stresses at their interfaces with neighboring plies, specially at interfaces away from the impact face which are, then, highly prone to delaminate. Not only such delaminations have important size, but they also become critical under CAI loads, both because of the relevant strain energy accumulated in the clustered plies and because of the relatively high interlaminar stresses that continue to be induced under CAI loads and promote further delamination propagation. Hence, BVID delamination between thick and inner neighbouring plies should always be mapped.

3. **The impact face sublaminate should consist of all plies down to the depth of permanent indentation (interfaced by a delamination mapped by an oval shape).**

   In general, delaminated interfaces at shallower depths than the value of permanent indentation are either implausible or non-critical for CAI strength, and may be disregarded. In support of the former assertion, Wisnom et al. [38] pointed out that right underneath the impact point delamination is suppressed due to the effect of out-of-plane compressive stresses. For the threshold of BVID, this corresponds to 1 mm through-thickness distance from the impact point. Hence, the first delamination to be mapped should be located after such distance from the impact face resulting in a sublaminate of thickness 1 mm or higher. An exception to this rule is made if at inferior but close distance, one or more laminae exist in loading direction, i.e. $0°$ plies. Due to the relatively high accumulated strain energy, the delamination of such a sublaminate from the main one may result in significant loss of stability. To account for this circumstance, the delamination of the $0°$ ply from the main sublaminate should be represented. If multiple $0°$ plies exist within the indentation depth, then only the delamination of the innermost one should be mapped, and under no circumstance a delamination in the two interfaces closer to the impact face need be modelled. The pre-delamination should be represented by an oval shape, with an aspect ratio of 2x1, with major axis of length equal to the diameter of the measured impact footprint.

4. **The backface sublaminate should consist of a single ply (interfaced by a delamination mapped by an oval shape).**

   The delamination of the backface ply is governed by the phenomenon of fibre splitting resulting in an elongated shape that overgrows the innermost LVI delaminations and is found to have a relevant effect on CAI behaviour. Hence, the backface sublaminate should consist of a single ply with delamination between the neighbouring sublaminate mapped as an oval shape with major axis doubling the diameter of the impact footprint, and an aspect ratio of 5x1.

5. **The second sublaminate from the backface should be modelled as consisting of two plies (interfaced by a delamination mapped by an oval shape).**

   To account for the fading influence of ply splitting towards the center of the impacted sample, the second sublaminate from the backface should be modelled as consisting of only two plies. The delamination towards the inside should be made oval with length of the major axis equalling 1.5 times the diameter of the impact footprint. Hwang and Huang [54] mentioned that a short delamination under a much larger delamination nearer the laminate surface, as defined by the previous guideline, has no effect on the CAI behaviour. The present research corroborates such observation for the case of relatively small delaminations underneath the impact point but leads to the opposite conclusion for the case of much larger delaminations close to the backface of the laminate.

6. **Once the above rules are satisfied, the remaining inner sublaminate should be divided into thinner sublaminates whose thicknesses depends on the thickness of the original laminate.**

   Hwang and Huang [54] observed that the local buckling load for multiple delaminated plies or sublaminates can be predicted by using a single sublaminate delaminated at a critical depth of the laminated coupon. This observation was supported by sensitivity studies conducted in the framework of the present research to investigate the number of plies that could reasonably be modelled by a single delaminated sublaminate. Based on the gathered information it was devised that, once the above rules are satisfied, the remaining inner sublaminate should be divided into thinner sublaminates whose thicknesses depend on the category of the original laminate:

(a) For thin laminates (laminates with less than 25 plies), the inner sublaminates should have 8-15% of the total original laminate thickness.

(b) For thicker laminates (laminates with 25 plies or more), the inner sublaminates should be further categorized into

   i. Sublaminates near the centre plane with 8-15 % of the original laminate thickness.

   ii. Sublaminates away from the centre plane with 15-20 % of the original laminate thickness.

In all these cases, the delamination profile should be circular with diameter equal to that of the impact footprint.

This rule was devised based on sensitivity analyses, and it does not necessarily result in the mapping of specific important or critical delaminations. Rather, it leads to the minimum amount, size and through-thickness distribution of delamination damage that needs to be represented in order to achieve accurate prediction of BVID tolerance.

The simplified BVID mapping resulting of the application of the above guidelines to the laminates analysed in this work is schematically represented in Figure 6 for comparison with the delamination profiles obtained experimentally by means of ultrasonic C-Scan. The detailed sublaminate-based configurations are given in Table 3.

4.3. Results of CAI simulation based on BVID mapping

Examples of simulations of deformation modes and delamination propagation resulting from using the methodology just described are shown in Figures 7 and 8. As a general trend, it was numerically predicted that delamination starts to propagate at the higher stages of compressive loading and mainly along the width-wise direction of the coupons, as experimentally observed by Chai et al. [55] among other authors. Such damage propagation accompanied the local buckling and bulging of the sublaminates and occurred within a relatively narrow loading window before the CAI specimen finally

Table 3: Sublaminate-based configurations for simulation of BVID tolerance. The locations of mapped delaminations are identified with '//'.

Laminate	**Sublaminate-based configuration**
181	$[\pm45/0//45_2//-45_2//90_2//-45_2//45_2//0/-45//45]$
181T	$[\pm45/0/\pm45//90/\pm45//45/-45_2//\pm45/45//$ $90/\mp45//0/-45//45]$
252	$[45/0/\text{-}45/90/45/0//\text{-}45/90//45/0//\text{-}45/90_2//-45/0/45//$ $90/\text{-}45/0//45,90//\text{-}45,0//45]$
351	$[45/0/\text{-}45/0/45/0//\text{-}45/90//45/90//\text{-}45/0_2//-45/90/45//$ $90/\text{-}45/0//45/0//\text{-}45/0//45]$
361	$[45/(0/\text{-}45)_2//45/0/-45/90/45_2//90/-45/0_2//-45/45_2//$ $\text{-}45/0_2//-45/90/45_2//90/-45/0/\pm45/0//-45/0//45]$

collapsed as the result of global or combined local-global buckling modes. By configuration, the thinner specimens of types 181 and 181T initially faced local buckling and collapsed by a global buckling mode whilst the thicker laminates 252, 351 and 361, initially developed local sublaminate buckling and failed by a mixture of both local and global buckling modes. Such buckling phenomena and their dependence on the thickness of the compressed specimen has been experimentally observed by other researchers [56]. At collapse, the delaminations grew rapidly towards the edges of the specimen. These predictions correlate well with the experimental observations gathered during the CAI tests and represented in Figure 8 for all configurations analyzed.

The progressive failure mechanisms explained above occur suddenly and close to specimen collapse, as corroborated by the high fidelity CAI simulations (see Figure 4). As a result, the load-displacement behaviors obtained experimentally and by means of simulations based on BVID mapping are fairly linear up to failure. The correlation between CAI strength results obtained by both methods (with and without applying Turons engineering solution for mesh coarsening [49]) is presented in Figure 9, which also indicates the obtained ranges of experimental results. The baseline virtual testing approach based on simplified delamination mapping is remarkably accurate, resulting in predictions within a 5% range of the average experimental values. The coarse mesh variant provides, in general, less accurate results but still within 90% accuracy.

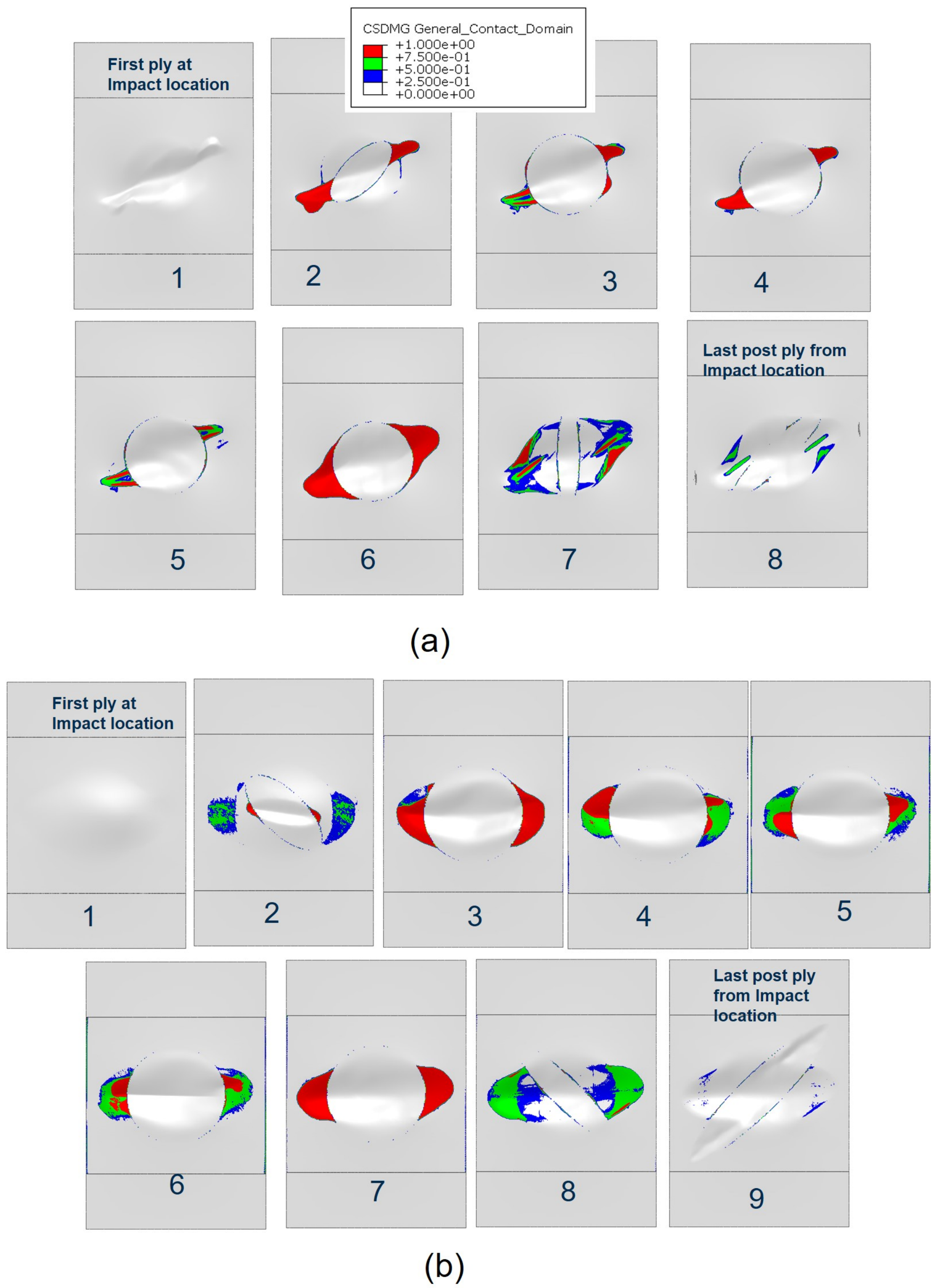

Figure 7: Simulated sublaminate deformations and delamination propagation at peak compressive load point: (a) configuration 181 (16 plies in 8 sublaminates); (b) configuration 252 (24 plies in 9 sublaminates).

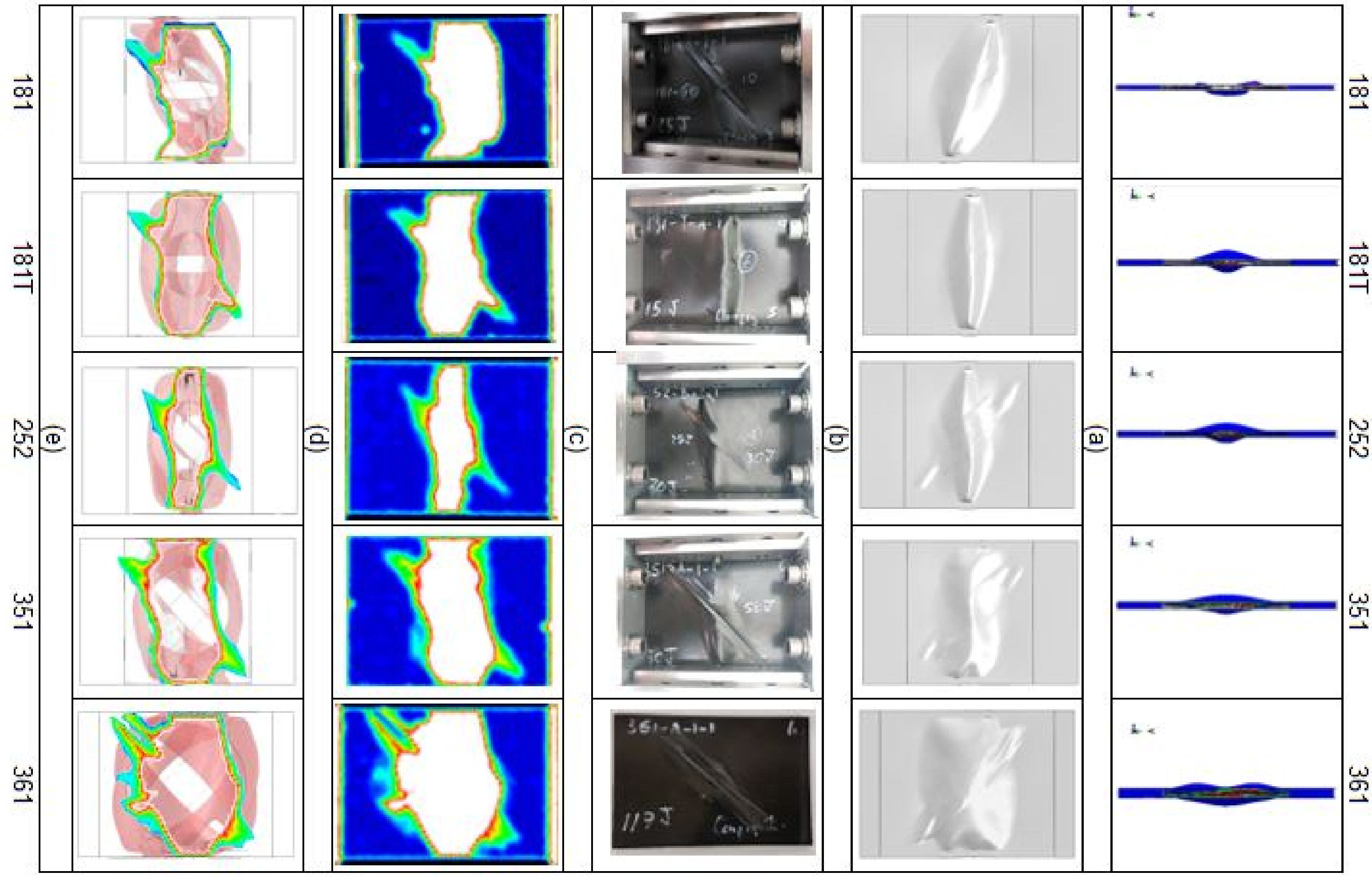

Figure 8: Correlation between experimental and numerical results obtained after collapse for different configurations subject to CAI: (a) Simulated deformation behaviour consisting of local, global or combined (mixed) buckling phenomena; (b) Simulated backface deformation; (c) Backface deformation and damage obtained experimentally; (d) Delamination profiles obtained by means of ultrasonic C-scan; (e) Simulated delamination profiles along with mapped C-scan.

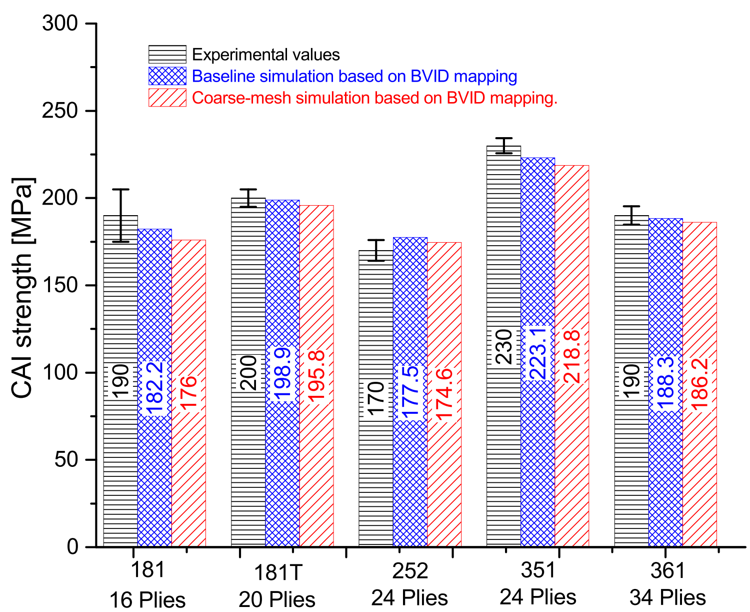

Figure 9: Comparison of CAI strength results obtained experimentally (ranges of experimental results indicated) and by means of simulation based on BVID mapping, with and without applying Turon's engineering solution for mesh coarsening [49].

5. Conclusions

This work proposes and validates an efficient numerical methodology to accurately predict the structural tolerance of composite laminates to BVID. It consists on mapping relevant BVID features, i.e. delaminations, onto an efficient CAI finite element model based on continuum shell element discretization. It is proposed that delaminations may be represented by simplified shapes, and that only the ones at critical through-thickness locations need to be mapped, allowing the clustering of several plies in a single shell layer. To aid the development and validation of the methodology, LVI and CAI experiments were carried on different laminate configurations based on the AS4/8552 carbon fibre-reinforced material system. Nonetheless, the guidelines proposed in this paper to perform delamination mapping into efficient CAI modelling are potentially applicable to a wide range of composite laminates.

The proposed approach can be seen as an alternative to the expensive CAI simulations that follow equally expensive high-fidelity LVI simulations, but can also be applied on experimental LVI results. Moreover, when applied on LVI virtual test results, the methodology leads not only to a simplification of the CAI step but also of the required LVI process simulation since this does not need to include the rebound of the impactor. This allows an acceleration of the full simulation of LVI plus CAI sequence by a factor of four. Considering the CAI step alone, two variants of the approach were presented: one allowing a speed-up factor above 6, in comparison with the alternative high-fidelity CAI virtual testing, and an accuracy level within the 5 % error range; and another allowing to speed-up analyses by over 50 times while obtaining values that differ as much as 10 % of the experimental results. In either case, the confidence and robustness of the predictions, although not competitive in computational cost, are substantially higher than for alternative analytic or semi-analytic models in the literature. Hence, this last type of analyses are very promising as a fast tool to asses BVID tolerance and predict material allowables in the aerospace industry environment and other alike.

Acknowledgements

The research leading to the developments described received funding of the project VIRTEST (Multiscale Virtual Testing of CFRP Samples), a collaboration between IMDEA Materials Institute and GKN Aerospace: Fokker. A. Baluch acknowledges the *Juan de la Cierva* fellowship (FJCI-2015-26212) supported by the Spanish Ministry of Economy, Industry and Competitiveness (MINECO), and the AMAROUT-II Marie Curie Action fellowship (PCOFUND-GA-2011-291803) supported by the European Commission. C.S. Lopes also acknowledges the support of MINECO through the *Ramón y Cajal* fellowship (grant RYC-2013-14271).

Data availability

The raw/processed data required to reproduce these findings cannot be shared at this time as the data also forms part of an ongoing study.

References

[1] A. T. Rhead, R. Butler, G. W. Hunt, Compressive strength of composite laminates with delamination-induced interaction of panel and sublaminate buckling modes, Composite Structures 171 (2017) 326 – 334.

[2] D. J. Thomas, Complexity of understanding the failure of aerospace composite structures, Journal of Failure Analysis and Prevention 16 (2016) 513–514.

[3] S. Abrate, Modeling of impacts on composite structures, Composite Structures 51 (2001) 129 – 138.

[4] L. Reis, M. de Freitas, Damage growth analysis of low velocity impacted composite panels, Composite Structures 38 (1997) 509 – 515. Ninth International Conference on Composite Structures.

[5] C. S. Lopes, O. Seresta, Y. Coquet, Z. Gūrdal, P. P. Camanho, B. Thuis, Low-velocity impact damage on dispersed stacking sequence laminates. part i: Experiments, Composites Science and Technology 69 (2009) 926 – 936.

[6] S. Hong, D. Liu, On the relationship between impact energy and delamination area, Experimental Mechanics 29 (1989) 115–120.

[7] E. Reddy, W. K. Binienda, Prediction of crack initiation in unidirectional composite beams subject to four-point bending, Composites Engineering 4 (1994) 703 – 714.

[8] D. Hull, Y. B. Shi, Damage mechanism characterization in composite damage tolerance investigations, Composite Structures 23 (1993) 99 – 120.

[9] S. Sanchez-Saez, E. Barbero, R. Zaera, C. Navarro, Compression after impact of thin composite laminates, Composites Science and Technology 65 (2005) 1911 – 1919.

[10] W. Cantwell, P. Curtis, J. Morton, An assessment of the impact performance of CFRP reinforced with high-strain carbon fibres, Composites Science and Technology 25 (1986) 133 – 148.

[11] J. Prichard, P. Hogg, The role of impact damage in post-impact compression testing, Composites 21 (1990) 503 – 511.

[12] S. Abrate, Impact on composite structures, Cambridge university press, New York (1998), 1986.

[13] V. Hawyes, P. Curtis, C. Soutis, Effect of impact damage on the compressive response of composite laminates, Composites Part A: Applied Science and Manufacturing 32 (2001) 1263 – 1270.

[14] G. Short, F. Guild, M. Pavier, The effect of delamination geometry on the compressive failure of composite laminates, Composites Science and Technology 61 (2001) 2075 – 2086.

[15] M. Abir, T. Tay, M. Ridha, H. Lee, On the relationship between failure mechanism and compression after impact (cai) strength in composites, Composite Structures 182 (2017) 242 – 250.

[16] R. Craven, L. Iannucci, R. Olsson, Delamination buckling: A finite element study with realistic delamination shapes, multiple delaminations and fibre fracture cracks, Composites Part A: Applied Science and Manufacturing 41 (2010) 684 – 692.

[17] M. Clarke, M. Pavier, Artificial damage techniques for low velocity impact in carbon fibre composites, Composite Structures 25 (1993) 113 – 120.

[18] L. E. Asp, S. Nilsson, S. Singh, An experimental investigation of the influence of delamination growth on the residual strength of impacted

laminates, Composites Part A: Applied Science and Manufacturing 32 (2001) 1229 – 1235.

[19] H. Suemasu, W. Sasaki, T. Ishikawa, Y. Aoki, A numerical study on compressive behavior of composite plates with multiple circular delaminations considering delamination propagation, Composites Science and Technology 68 (2008) 2562 – 2567.

[20] X. Wang, I. Pont-Lezica, J. Harris, F. Guild, M. Pavier, Compressive failure of composite laminates containing multiple delaminations, Composites Science and Technology 65 (2005) 191 – 200.

[21] Z. Aslan, M. Sahin, Buckling behavior and compressive failure of composite laminates containing multiple large delaminations, Composite Structures 89 (2009) 382 – 390.

[22] R. S. Choudhry, A. T. Rhead, M. W. Nielsen, R. Butler, A plate model for compressive strength prediction of delaminated composites, Composite Structures 210 (2019) 509 – 517.

[23] G. Minak, M. Fotouhi, M. Ahmadi, 6 - low-velocity impact on laminates, in: V. V. Silberschmidt (Ed.), Dynamic Deformation, Damage and Fracture in Composite Materials and Structures, Woodhead Publishing, 2016, pp. 147 – 165.

[24] V. Obdrzālek, J. Vrbka, On buckling of a plate with multiple delaminations, Engineering Mechanics 17 (2010) 37–47.

[25] M.-K. Yeh, C.-M. Tan, Buckling of elliptically delaminated composite plates, Journal of Composite Materials 28 (1994) 36–52.

[26] N. Hu, H. Fukunaga, H. Sekine, K. M. Ali, Compressive buckling of laminates with an embedded delamination, Composites Science and Technology 59 (1999) 1247 – 1260.

[27] E. González, P. Maimí, A. Turon, P. Camanho, J. Renart, Simulation of delamination by means of cohesive elements using an explicit finite element code, Computers, Materials and Continua 9 (2009) 51–92.

[28] C. S. Lopes, S. Sádaba, C. González, J. Llorca, P. Camanho, Physically-sound simulation of low-velocity impact on fiber reinforced laminates,

International Journal of Impact Engineering 92 (2016) 3 – 17. Impact Loading on Lightweight Structures.

[29] W. Tan, B. G. Falzon, L. N. Chiu, M. Price, Predicting low velocity impact damage and compression-after-impact (cai) behaviour of composite laminates, Composites Part A: Applied Science and Manufacturing 71 (2015) 212 – 226.

[30] E. González, P. Maimí, P. P. Camanho, A. Turon, J. Mayugo, Simulation of drop-weight impact and compression after impact tests on composite laminates, Composite Structures 94 (2012) 3364 – 3378.

[31] C. S. Lopes, P. P. Camanho, Z. Gūrdal, P. Maimí, E. Gonzlez, Low-velocity impact damage on dispersed stacking sequence laminates. part ii: Numerical simulations, Composites Science and Technology 69 (2009) 937 – 947.

[32] O. Falcó, R. Ávila, B. Tijs, C. S. Lopes, Modelling and simulation methodology for unidirectional composite laminates in a virtual test lab framework, Composite Structures 190 (2018) 137 – 159.

[33] ASTM-D7136/D7136M-12., Standard test method for measuring the damage resistance of a fiber-reinforced polymer matrix composite to a drop-weight impact event., ASTM International standard; West Conshohocken PA, USA; (2012).

[34] AITM1-0010., Fibre reinforced plastics, determination of compression strength after impact., AITM, Airbus Test Method, Engineering directorate 31707 Blagnac Cedex France (2005).

[35] F. Romano, F. D. Caprio, U. Mercurio, Compression after impact analysis of composite panels and equivalent hole method, Procedia Engineering 167 (2016) 182 – 189. International Symposium on Dynamic Response and Failure of Composite materials, Draf2016.

[36] C. Kassapoglou, Design and Analysis of Composite Structures: With Applications to Aerospace Structures, John Wiley & Sons Ltd, 2013.

[37] S. Petit, C. Bouvet, A. Bergerot, J.-J. Barrau, Impact and compression after impact experimental study of a composite laminate with a cork

thermal shield, Composites Science and Technology 67 (2007) 3286 – 3299.

[38] M. R. Wisnom, The role of delamination in failure of fibre-reinforced composites, Philosophical transactions. Series A, Mathematical, physical, and engineering sciences (2012).

[39] ASTM-D7137/D7137M-17., Standard test method for compressive residual strength properties of damaged polymer matrix composite plates., ASTM International standard; West Conshohocken PA, USA; (2017).

[40] ABAQUS, version 6.14 online documentation. Analysis users manual, SIMULIA Inc., Dassault Systmes, ABAQUS, 2013.

[41] P. Maimí, P. P. Camanho, J. Mayugo, C. Dávila, A continuum damage model for composite laminates: Part i constitutive model, Mechanics of Materials 39 (2007) 897 – 908.

[42] P. Maimí, P. P. Camanho, J. Mayugo, C. Dávila, A continuum damage model for composite laminates: Part ii computational implementation and validation, Mechanics of Materials 39 (2007) 909 – 919.

[43] W. Ramberg, W. R. Osgood, Description of stressstrain curves by three parameters, National Advisory Committee For Aeronautics (1943). Technical Note No. 902.

[44] G. Catalanotti, P. P. Camanho, A. Marques, Three-dimensional failure criteria for fiber-reinforced laminates, Composite Structures 95 (2013) 63 – 79.

[45] P. P. Camanho, C. G. Dávila, Mixed-mode decohesion finite elements for the simulation of delamination in composite materials, NASA/TM-2002211737, pp. 137, 2002.

[46] M. L. Benzeggagh, M. Kenane, Measurement of mixed-mode delamination fracture toughness of unidirectional glass/epoxy composites with mixed-mode bending apparatus, Composites Science and Technology 56 (1996) 439–449.

[47] Z. P. Bažant, B. H. Oh, Crack band theory for fracture of concrete, Matériaux et Construction 16 (1983) 155–177.

[48] X. Sun, S. Hallett, Failure mechanisms and damage evolution of laminated composites under compression after impact (cai): Experimental and numerical study, Composites Part A: Applied Science and Manufacturing 104 (2018) 41 – 59.

[49] A. Turon, C. Dávila, P. P. Camanho, J. Costa, An engineering solution for mesh size effects in the simulation of delamination using cohesive zone models, Engineering Fracture Mechanics 74 (2007) 1665 – 1682.

[50] J. R. Rice, The mechanics of earthquake rupture, Proceedings of the international school of physics Enrico Fermi, Course 78, 1979, Italian Physical Society/North-Holland, Amsterdam (1979) 555 – 649.

[51] B. Vieille, V. Casado, C. Bouvet, Influence of matrix toughness and ductility on the compression-after-impact behavior of woven-ply thermoplastic- and thermosetting-composites: A comparative study, Composite Structures 110 (2014) 207 – 218.

[52] V. Obdrz̄álek, J. Vrbka, On the applicability of simple shapes of delamination in buckling analysis, Composites Part B: Engineering (2011) 538 – 545.

[53] L. Melin, J. Schōn, Buckling behaviour and delamination growth in impacted composite specimens under fatigue load: an experimental study, Composites Science and Technology 61 (2001) 1841 – 1852.

[54] S.-F. Hwang, S.-M. Huang, Postbuckling behavior of composite laminates with two delaminations under uniaxial compression, Composite Structures 68 (2005) 157 – 165.

[55] H. Chai, W. G. Knauss, C. D. Babcock, Observation of damage growth in compressively loaded laminates, Experimental Mechanics 23 (1983) 329–337.

[56] V. Obdrz̄álek, Simulation of interlaminar and intralaminar damage in polymer-based composites for aeronautical applications under impact loading, PhD thesis (2010) 40 – 41.